

1 **Publised in Journal of Hydrology 405 (2011) 474–487**

2

3 **A Conceptual hydrodynamic model of a geological**  
4 **discontinuity in hard rock aquifers: example of a quartz**  
5 **reef in granitic terrain in South India**

6

7 Benoît DEWANDEL<sup>1\*</sup>, Patrick LACHASSAGNE<sup>1,2</sup>, Faisal K. ZAIDI<sup>3,4</sup>, and Subash CHANDRA<sup>2</sup>

8

9

10 1- BRGM, Water Division, Resource Assessment, Discontinuous Aquifers Unit, 1039 Rue  
11 de Pinville, 34000 Montpellier, France; [b.dewandel@brgm.fr](mailto:b.dewandel@brgm.fr); (\*Corresponding author).

12 2- Now at Danone Waters France, 11 av. G. Dupas, BP 87, 74503 Evian-les-Bains Cedex,  
13 France; [Patrick.lachassagne@danone.com](mailto:Patrick.lachassagne@danone.com).

14 3- National Geophysical Research Institute, Indo-French Centre for Groundwater  
15 Research, Uppal Road, 500 007 Hyderabad, India; [schandra75@gmail.com](mailto:schandra75@gmail.com).

16 4- Now at Department of Geology, College of Science, King Saud University, Riyadh,  
17 Kingdom of Saudi Arabia; [fk.zaidi@gmail.com](mailto:fk.zaidi@gmail.com).

18

19

20 **Abstract**

21 The structure and hydrodynamic properties of geological discontinuities and of a deeply  
22 weathered granite aquifer near these structures are described on the basis of geological,  
23 geophysical and hydrodynamic investigations in two sites of South India located along a 20-  
24 40-metre-wide quartz reef intruding a weathered Archean biotite granite. One of the two sites  
25 also comprises a metre-wide dolerite dyke.

26 Weathering processes appear to be at the origin of fissures development and of a related  
27 enhanced local hydraulic conductivity, both in the quartz reef and in the surrounding granite.

28 The weathering profile in the granite (saprolite and fissured layer) is characterized by an  
29 abrupt deepening of the weathered layers in the granite near the contact and in the quartz reef  
30 itself. Therefore, the weathering profile shows a ‘U’-shape geometry with, among others, the  
31 verticalization of the granite’s fissured layer. The hydraulic conductivity of this verticalized

32 layer is on average  $5 \times 10^{-6}$  m/s and storativity about  $10^{-3}$  (-). The hydraulic conductivity of  
33 the fissured quartz is 4 to  $6 \times 10^{-6}$  m/s and its storativity about 3 to  $5 \times 10^{-4}$  (-). Both media are  
34 also characterized by a matrix hydraulic conductivity ( $10^{-7}$  to  $10^{-9}$  m/s) and by a significant  
35 heterogeneity in hydrodynamic properties that generates preferential flow paths along the sub-  
36 vertical fissures parallel to the reef axis. A special attention has been paid for characterizing  
37 this heterogeneity.

38 The weathering of the dolerite dyke, however, results in a local low hydraulic conductivity,  
39 which consequently does not enhance either the thickness of weathered granite layers or its  
40 hydraulic conductivity.

41 The obtained results complete the conceptual hydrogeological model developed for weathered  
42 granite aquifers in characterizing the relationships between weathering processes and  
43 hydrodynamic properties near geological discontinuities.

44

45 Key words: hard rock, discontinuity, granite, weathering, hydrodynamic properties,  
46 heterogeneity in hydraulic conductivity

47

## 48 **1. Introduction**

49 Hard rocks (plutonic, metamorphic rocks) form part of the basement of continents and, as  
50 such, occupy large areas throughout the World (Africa, South and North America, India,  
51 Europe, Asia, Australia, etc.). Groundwater resources in aquifers (HRA) are generally low in  
52 terms of available discharge per well (from a few to a few tens of  $\text{m}^3/\text{h}$ ) compared to those  
53 from porous, karst, and volcanic aquifers. However, HRA are geographically widespread and  
54 thus well-suited for water supply to scattered populations and small to medium-size towns, or  
55 suburbs of larger cities. Their groundwater resources largely contribute to economic  
56 development, especially in regions exposed to arid and semiarid climatic conditions where  
57 surface-water resources are limited as, for example, in Africa and in India (Uhl and Sharma,  
58 1978; Gustafson and Krásný, 1994; Houston and Lewis, 1998). In such regions, HRA  
59 commonly are the only available perennial water resource, supplying the population as well as  
60 the agricultural and industrial sectors. However, the knowledge of such aquifers, e.g., their  
61 geometry, their hydraulic properties, etc., is currently meagre and needs to be improved.

62 Significant advances have recently been made in the geological and hydrogeological  
63 characterization of such complex aquifers (Omorinbola, 1982; Owoade, 1995; Chilton and  
64 Foster, 1995; Taylor and Howard, 2000; Lachassagne et al., 2001; Wyns et al., 2004,

65 Maréchal et al., 2004; Dewandel et al., 2006; Ayraud et al., 2008; Courtois et al., 2010;  
66 Lachassagne et al., 2011). These studies show that the geometry and the hydrodynamic  
67 properties of HRA mainly result from deep weathering processes of the parent rock. Such  
68 processes involve biogeochemical hydrolysis of the minerals constituent of the rocks and their  
69 mineral transformation under new surface conditions, mainly into clay-rich materials (Tardy,  
70 1971, 1993, 1998; Nahon, 1991). Additionally, these processes are controlled by the regional  
71 geodynamical history, which can lead to multiphase weathering profiles because of  
72 alternating erosion and weathering phases (Taylor and Howard, 2000; Dewandel et al., 2006).

73 In granite-type rocks (e.g. granite, gneiss), a typical weathering profile comprises two main  
74 stratiform layers sub-parallel to the paleo-surface contemporaneous of the weathering  
75 processes (Fig.1; Chilton and Smith-Carrington, 1984; Chilton and Foster, 1995; Wyns et al.,  
76 1999 and 2004, Krásný and Sharp, 2007; Maréchal et al., 2007, and others). From the top  
77 downward, they are (i) the **saprolite layer**, a clay-rich material usually characterized by low  
78 hydraulic conductivity, and (ii) the fissured layer characterized by dense horizontal fissuring  
79 within the first few metres and a depth-decreasing of the sub-horizontal and sub-vertical  
80 fissure sets (Howard et al., 1992; Houston and Lewis, 1998; Maréchal et al., 2004; Wyns et  
81 al., 2004; Dewandel et al., 2006). This last layer usually assumes the transmissive function of  
82 the aquifer. The **underlying unfissured and fresh basement** is only locally permeable where  
83 deep fractures occur, but these conductive zones are much less dense than in the overlying  
84 fissured layer and their hydrodynamic properties are highly variable (Pickens et al., 1987;  
85 Blomqvist 1990; Walker et al., 2001; Kuusela et al., 2003; Cho et al., 2003). Flow can be  
86 fractionalized, i.e. controlled by the orientation of the fracture network (Leveinen et al.,  
87 1998).

88 As a consequence, where the formation is not affected by geological discontinuities, such as  
89 faults, veins or dykes, and exposed to deep weathering processes, the saprolite and the  
90 fissured layers together make up a composite aquifer of up to 100 m thick (Fig.1).  
91 Hydrogeologically, this medium can be considered as a multilayer system where each layer is  
92 characterized by its own specific and quite homogeneous hydrodynamic properties. This  
93 relative “homogeneity” allows several practical applications (Lachassagne et al., 2011),  
94 among which aquifer budgeting (Maréchal et al., 2006) or the development of Decision  
95 Support Tools (Dewandel et al., 2008, 2010). However, where the granite is intruded by  
96 quartz, pegmatite or aplite veins, dolerite dykes, or younger granite, or affected by tectonic  
97 faults, the layers geometry and their hydrodynamic properties may substantially differ from

98 the above-presented conceptual model. Locating such heterogeneities in hard rocks,  
99 commonly resulting from lineament analysis and/or geophysical surveys, constitutes the  
100 backbone of borehole siting, as major discontinuities and their intersections are often assumed  
101 to be strong indicators of a groundwater resource (Mabee et al., 1994; Minor et al., 1995;  
102 Sander et al., 1997; Chandra et al., 2006; Sander, 2007). However, such structures do not  
103 necessarily give impressive results in terms of well productivity (Sander, 2007); probably  
104 because at present their hydrogeological properties in terms of hydrodynamics and geometry  
105 are insufficiently understood.

106 The objective of the present paper is to improve the understanding of the geometry and  
107 hydrodynamic properties of such geological discontinuities, through the case-study of a 20 to  
108 40-metre-thick quartz vein intruding granite that was exposed to deep weathering processes.  
109 This work has led to a 3-D conceptual hydrogeological model of this structure, on the basis of  
110 geological and geophysical surveys, and hydraulic tests carried out on two pilot sites equipped  
111 with a total of 21 boreholes (Fig. 2, Maheshwaram area, Ranga Reddy District, Andhra  
112 Pradesh, India).

113

## 114 **2. Geological setting**

115 The studied sites are located 40 km south of Hyderabad (Andhra Pradesh, India). The area is  
116 characterized by a relatively flat topography with altitudes ranging from 670 to 590 m above  
117 mean sea level. The region experiences a semi-arid climate controlled by the periodicity of the  
118 monsoon (rainy season: June to October). Mean annual precipitation is about 750 mm, of  
119 which more than 90% falls during the monsoon season.

120 The area is underlain by Archean biotite granite that is locally intruded by leucocratic granite.  
121 These granites are affected by deep in-situ multi-phase weathering-and-erosion processes  
122 (Dewandel et al., 2006). At the regional scale, the weathered horizons more or less follow the  
123 current topography and, from top to bottom, are composed of:

- 124 - A 1-3-m thick layer of sandy regolith, locally capped by a lateritic crust (<50 cm);
- 125 - A 10-15-m thick layer of laminated saprolite;
- 126 - And, a 15-20-m thick layer of fissured granite, where weathered granite and clay  
127 minerals can partially fill the fissures.

128 The granites are locally intruded by up to 40-m-wide quartz veins (Archean in age) and metre-  
129 wide dolerite dykes (2.5 to 1.6 Ga; G.S.I. 2002; Fig. 2). Quartz reefs systematically occupy  
130 positive relief in the area. In order to investigate the impact of such discontinuities on the

131 weathering-profile structure and its hydrodynamic properties, geological and geophysical  
 132 investigations were carried out on two pilot sites: “IFP 1” and “Kothur” (Figs. 2 and 3). The  
 133 two sites, separated by 7 km, are located along the same sub-vertical and north-south  
 134 decametre-wide quartz reef.

135 Electrical Resistivity Tomography profiles were carried out on the two sites for siting the 21  
 136 boreholes used in the study (Chandra et al., 2010). Five ERT profiles were carried on the  
 137 Kothur site and one on the IFP1 site. All ERT profiles show that the quartz reef, particularly  
 138 at depth, is characterized by lower resistivities than the surrounding granite, which is  
 139 attributed to a more developed fissure network at depth (see supplemental material). At Kothur  
 140 six boreholes were drilled in the central area and in the pinch-out zone of the quartz reef and 5  
 141 in the surrounding granite (Fig. 3a and 3b). The ten IFP1 boreholes were located within the  
 142 granite in the pinch-out zone of the quartz reef and near a metre-wide dolerite dyke (Fig. 3a)  
 143 that was intersected by two boreholes (IFP 1-4 and 1-8). The depth of the 21 boreholes ranges  
 144 between 35 and 91.4 m (Table 1); detailed geological logs were prepared from drill cuttings  
 145 (see supplemental material). At IFP1 site, two pre-existing farmer’s wells (bw1 and bw2,  
 146 Fig. 3a) drilled within the granite are also present, but their exact depth is unknown.

147 The combination of the geophysical and the geological data allowed characterizing both the  
 148 structure of the geological formations and the geometry of the weathering profile near the  
 149 intrusion. Geological cross-sections perpendicular and parallel to the reef for the two sites  
 150 clearly show that the weathering profile is significantly deepened near the quartz reef (Figs  
 151 4a, b and c). At the outcrop scale, the orientation of major fissures (metre to decametre wide)  
 152 in the quartz reef was measured (see supplemental material). The fissures are mostly sub-  
 153 vertical and organized in two main sub-orthogonal sets, one sub-parallel (N000 90°) to the  
 154 quartz vein and the second sub-orthogonal (N100 90°) to it. A few sub-horizontal fissures  
 155 were also observed, but due to the relatively flatness of the outcrops their number is probably  
 156 underestimated. Within the first ten metres from surface, the quartz is highly weathered and  
 157 densely fissured from centimetre to decametre scale. However, near the contact with the  
 158 granite, i.e. on the sides of the quartz reef and in the pinch-out zones, this highly weathered  
 159 and fissured material can reach up to 50 m depth (Figs. 4b and c). Near the quartz reef, the  
 160 granite is also characterized by an important deepening of the weathering profile. On average,  
 161 saprolite thickness increases by a factor 1.5 to 3 and the fissured layer by a factor 3 to 5,  
 162 compared to the zone not affected by the intrusion. Locally, the bottom of the fissured layer  
 163 can reach more than 70 m depth, whereas farther from the quartz reef the weathering profile  
 164 in the granite stops at few tens of metres from the surface (Figs. 4).

165 The IFP1 sub-vertical and metre-wide dolerite dyke sub-parallel to the quartz reef is highly  
 166 weathered within the first 6 m from the surface (clayey material), then poorly fissured up to  
 167 15 m, and finally hard and compact. Near this dyke there is no-evidence of a deepening of the  
 168 weathering front and of the development of a local deeper fissuring.

169 Previous studies (Maréchal et al., 2004; Dewandel et al., 2006) showed the relative  
 170 homogeneity of the hydrodynamic properties of the weathered/fissured hard-rock aquifers  
 171 where the granite is not affected by such discontinuities. Several questions now arise: are the  
 172 hydrodynamic properties different in such verticalized weathered-fissured layers? Does the  
 173 preferential orientation of fissures in the quartz reef play a role? What is the hydrogeological  
 174 conceptual model of these discontinuities? To try and provide answers to these questions, slug  
 175 tests and pumping tests were performed on both sites.

176

### 177 **3. Hydrodynamic investigations**

#### 178 **3.1. Slug tests**

179 Twenty-one slug tests were carried out in the boreholes of both pilot sites and were  
 180 interpreted using the Bouwer and Rice (1976) technique for unconfined aquifers with  
 181 completely or partially penetrating wells. The obtained distribution of hydraulic  
 182 conductivities constitutes a preliminary estimate of the hydraulic conductivity of the  
 183 weathered layers in the granite and in the quartz aquifers near the wells (Fig. 5).

184 Near the quartz reef, the hydraulic conductivity of the fissured granite ranges from  $8.5 \times 10^{-8}$   
 185 m/s to  $8.8 \times 10^{-6}$  m/s with a geometrical mean of  $2.4 \times 10^{-6}$  m/s and a standard deviation of 0.6  
 186 computed on a logarithmic scale ( $\log K_{\text{slug}}: -5.6 \pm 0.6$ ). In the quartz reef, values are similar and  
 187 range from  $5.0 \times 10^{-8}$  m/s up to  $1.6 \times 10^{-5}$  m/s with a geometrical mean of  $2.6 \times 10^{-6}$  m/s and a  
 188 standard deviation on a log scale of 1.0 ( $\log K_{\text{slug}}: -5.6 \pm 1.0$ ). Within these distributions, a  
 189 small population of two boreholes (IFP30-3,  $K=8.5 \times 10^{-8}$  m/s and IFP30-6,  $K=5.1 \times 10^{-8}$  m/s)  
 190 with hydraulic conductivities of less than  $10^{-7}$  m/s corresponds to poorly fissured granite and  
 191 quartz and is possibly representative of the matrix hydraulic conductivity. The hydrodynamic  
 192 properties of the dolerite dyke were not explored since no water contribution was observed  
 193 during drilling despite the shallow water-table (4 m from surface). The hydraulic conductivity  
 194 distributions in the quartz reef and in the nearby granite seem to follow near-log normal  
 195 distributions, similar to that of the stratiform fissured layer far from discontinuities in the  
 196 same granite (geometric mean of  $4.4 \times 10^{-6}$  m/s, Maréchal et al., 2004). However, the spatial  
 197 distribution of hydraulic conductivity in the quartz reef is highly variable and is closely linked

198 with the degree of weathering. Indeed, at the centre of the quartz reef, where a high grade of  
 199 weathering and fissuring only affects the first metres below surface, the quartz is  
 200 characterized by quite low hydraulic conductivities (IFP30-1, 30-6;  $K < 5 \times 10^{-7}$  m/s), whereas  
 201 it is significantly more permeable near the contact with granite (e.g., IFP30-9, 30-10, 30-11;  
 202  $K > 10^{-5}$  m/s). This shows that most of the conductive fissures develop in the contact zones (i.e.  
 203 sides and pinch-out zones), whereas the heart of the reef is poorly fissured.  
 204 For the granite, no clear relationship between hydraulic conductivity and location relative to  
 205 the quartz reef is found, suggesting that both near and far from the discontinuity the fissured  
 206 layer of the granite exhibits similar properties.

207

## 208 **3.2. Pumping tests**

### 209 ***3.2.1. Brief description of the method used***

210 The interpretation of pumping tests in such fissured aquifers commonly is a difficult task, as  
 211 groundwater flow can be fractionalized (Black, 1994; Le Borgne et al., 2004) and controlled  
 212 by the hydraulic conductivity of fissures, their density and orientation, and also their  
 213 relationships with low-hydraulic-conductivity blocks or matrix (e.g. Maréchal et al., 2004; Le  
 214 Borgne et al., 2006). In order to reveal the various aspects of the hydrodynamic properties of  
 215 such a complex medium and to appropriately model the pumping test, a special attention has  
 216 been paid to diagnosing of the tests prior to their modelling. Diagnoses were based on the  
 217 analysis of derivative drawdown curves on log-log plots that allows flow-regime  
 218 identification (Bourdet et al., 1983, 1989; Ehlig-Economides, 1988; Spane and Wurstner,  
 219 1993, Renard et al., 2009). The tests were then interpreted with WinISAPE (BRGM software)  
 220 and WTFM (Lods and Gouze, 2004). Table 2 presents the main characteristics of the pumping  
 221 tests.

222 The observations and models were visually matched on both drawdown and derivative curves.  
 223 The sensitivity of the hydrodynamic-parameter estimates was inferred from several fitting  
 224 tests: it is less than 15% on average for the hydraulic conductivity and less than 20% on  
 225 average for storativity. Since 34 curves were interpreted for the study, only a few curves are  
 226 presented here (Fig. 6a, b and c).

227

### 228 ***3.2.2. Pumping tests at the Kothur site***

229 Three non-simultaneous pumping tests were performed, two within the quartz reef (IFP30-5  
 230 and IFP30-10) and one within in the stratiform fissured layer of the granite (IFP30-4) at a  
 231 quite large distance from the quartz vein (Fig. 3b; Tables 3 to 5).

232 Pumping in IFP30-5 revealed spherical flow during the early stage of pumping ( $-1/2$  slope of  
233 derivative curve;  $t < 100$  min; Fig. 6a) that is typical of a borehole partially penetrating the  
234 aquifer. As this well intersects about 30 to 40 m of fractured quartz (Fig. 4c), this diagnosis  
235 suggests that IFP30-5 is located in a zone where the aquifer is relatively thin compared to  
236 where the drawdown progresses. This is corroborated by the geological observations, which  
237 show that the thickness of the weathered/fissured zone increases up to 70 m depth north of the  
238 site (Fig. 4c). The whole data set from pumping and observation wells has been interpreted  
239 with the Hantush model (partially penetrating aquifer with vertical anisotropy in hydraulic  
240 conductivity; Hantush, 1961; Fig. 6a). Estimated hydrodynamic parameters are of the same  
241 order of magnitude and relatively close from one well to the next with, however, a variability  
242 in the estimates and particularly those for hydraulic conductivity and storativity (Table 3); this  
243 point will be discussed later. On average, the hydraulic conductivity is  $4.0 \times 10^{-6}$  m/s, the  
244 storativity about  $3.2 \times 10^{-4}$  (-) and the aquifer thickness is estimated to be about 100 m. The  
245 computed aquifer thickness appears slightly overestimated compared to reality (about 70 m),  
246 which we explain by the uncertainty of the real productive length in wells (screened thickness  
247 on Table 3) but also by the use of the Hantush model that considers a well that partially  
248 penetrates the aquifer whereas IFP30-5 is located in a pinch-out zone of the aquifer. The  
249 vertical anisotropy ratio in hydraulic conductivity ( $K_x/K_z$ ) is about 3 and probably reveals a  
250 depth-decreasing hydraulic conductivity due to a depth-decreasing density of fissures.

251 The test performed in IFP30-10 revealed a dual porosity behaviour (Fig. 6b). The overall data  
252 set has thus been interpreted with a dual porosity model. Two observation wells (IFP30-6 and  
253 30-7) were interpreted in the matrix, the others being in the fissure network (Table 4; Fig. 6b).  
254 Compared to the previous pumping test, spherical flow is absent showing that IFP30-10  
255 intersected most of the aquifer thickness and thus that the bottom of the aquifer is close to  
256 70 m deep. The estimated hydrodynamic parameters are consistent with the ones obtained in  
257 IFP30-5 and of the same order of magnitude (Table 4). This test gives complementary  
258 information on the hydraulic parameters of the quartz reef aquifer. On average, the hydraulic  
259 conductivity of the aquifer is  $6.2 \times 10^{-6}$  m/s, the storativity is about  $4.6 \times 10^{-4}$  (80% in the  
260 matrix and 20% in the fissures), and the matrix hydraulic conductivity is about  $2.4 \times 10^{-9}$  m/s.  
261 Variability in hydraulic conductivity and storativity estimates was also noted and will be  
262 discussed later.

263 The third test at Kothur (IFP30-4) characterises the stratiform fissured layer of the granite not  
264 affected by the reef. Only two observation wells reacted to the test (IFP30-7 and 30-8). The  
265 aquifer behaviour is typical of a dual-porosity medium and the hydrodynamic parameters are

266 very similar (Table 5). The hydraulic conductivity of the fissured granite is on average  $6.4 \times$   
 267  $10^{-6}$  m/s, the storativity is about  $7.2 \times 10^{-3}$  (98% in the matrix, 2% in the fissures), and the  
 268 matrix hydraulic conductivity is about  $3.0 \times 10^{-9}$  m/s.

269

### 270 **3.2.3. Pumping tests at the IFP1 site**

271 At the IFP1 site, wells were drilled in the granite, in the pinch-out zone of the quartz reef  
 272 (Fig. 3a). A pumping test in IFP1-6 revealed the channelized structure of the aquifer after a  
 273 few minutes of pumping (1/2 slope of the derivative curve on Fig. 6c). This is consistent with  
 274 the geological information and particularly the 'U'-shape geometry of the aquifer (Fig. 4a).  
 275 Therefore, a Theis model combined with two parallel no-flow boundaries was used for the  
 276 interpretation (Fig. 6c). Several hypotheses were tested for the orientation of the two no-flow  
 277 boundaries. The best result, which was constrained by the modelled drawdowns for the 10  
 278 wells, was obtained for a direction sub-parallel to the quartz reef (N195). Aquifer parameters  
 279 are quite homogeneous (Table 6) with, however, a certain variability in the hydraulic  
 280 conductivity and storativity values. The average hydraulic conductivity is  $4.5 \times 10^{-6}$  m/s and  
 281 the average storativity  $7.8 \times 10^{-4}$  (-). Distances from IFP1-6 to the two no-flow boundaries are  
 282 on average 20 and 44 m respectively, which is consistent with the geological information  
 283 (Fig. 4a). The nearest no-flow boundary, located east of IFP1-6 ( $d_1=19.5 \pm 9$  m), corresponds  
 284 to the dolerite dyke while the farthest boundary is the western limit of the verticalized fissured  
 285 layer of the granite ( $d_2=44.3 \pm 2$  m).

286 Nevertheless, some discrepancies to this overall interpretation are found. Interpretation of the  
 287 observation well IFP1 data gives higher distances to limits, and particularly to the farthest one  
 288 (138 m) because of the very low storage coefficient computed for this well ( $S=7 \times 10^{-5}$ ;  
 289  $\text{dist.limit}=1.5[Tt/S]^{1/2}$ ; Jacob, 1947). This low value compared to the average found for the  
 290 site is probably caused by a highly conductive zone connecting this well to the pumping well  
 291 thus enhancing a rapid pressure transfer between the two wells, quicker than the general one  
 292 found at the site scale. The re-computation of the distance to limits with the average storage  
 293 coefficient found at the site scale gives results that are consistent with the ones found in the  
 294 other wells (Table 6). Compared to other wells, drawdown at IFP 1-3, 1-4 and 1-8 was very  
 295 low ( $<0.8$  m) which is explained by their location outside the permeable channel (Figs. 3a and  
 296 4a). The data were interpreted with the Theis model, but the estimated hydraulic parameters,  
 297 K and S, are non-realistic and differ by several orders of magnitude from the ones obtained in  
 298 other wells. These wells are thus located in an aquifer that is poorly connected to the

299 permeable channel. These records nevertheless show that the dolerite dyke no-flow boundary  
300 is not a completely impervious limit, but rather a low-permeability barrier.

301 The second test performed in IFP1-8 produced drawdown in only a few observation wells  
302 (IFP1-4 and farmer wells BW1 and 2; Fig. 3a). The eight other observation wells did not react  
303 to pumping, corroborating the presence of a no-flow boundary between IFP1-8 and IFP1-5,  
304 i.e. the dolerite dyke. This test reinforces the scheme deduced from the test at IFP1-6. The  
305 interpretations give similar results, with an average hydraulic conductivity of the aquifer at  
306  $1.5 \times 10^{-5}$  m/s and a storativity,  $S$ , of about  $2.2 \times 10^{-4}$  (-).

307

### 308 **3.3. Anisotropy and heterogeneity in hydraulic conductivity**

309 Fissure measurements on the quartz-reef outcrops at IFP1 and Kothur sites show that the  
310 fissure network is well organized with dominant sets that are sub-parallel and sub-orthogonal  
311 to the reef axis (see supplemental material). Moreover, the variability in hydraulic  
312 conductivity - particularly within the quartz reef ( $\log K_{\text{slug}}: -5.6 \pm 1.0$ ) - is high because of the  
313 variation in the weathering grade. As a consequence, anisotropy and heterogeneity in  
314 hydraulic conductivity are expected and may explain the variability in hydraulic conductivity  
315 and storativity deduced from the pumping tests.

316

#### 317 **3.3.1. Homogeneous and anisotropic aquifer: the stratiform horizontal fissured layer**

318 In an ideal homogeneous and anisotropic aquifer, the hydraulic conductivity on the horizontal  
319 plane can be represented by a tensor characterized by two orthogonal major and minor axes.  
320 When a pumping test is performed, the drawdown geometry forms an ellipse that reflects the  
321 anisotropy ratio (Hantush, 1966; Hantush and Thomas, 1966; Ramey, 1975; Neuman et al.,  
322 1984). The estimation of the anisotropy ratio and of the major and minor hydraulic  
323 conductivity orientations requires several observation wells located at various angle from the  
324 two anisotropy axes (e.g. Neuman et al., 1984). For such a medium and considering an  
325 isotropic storativity, drawdown curves from observation wells will all be characterized by the  
326 same semi-log slope (Jacob's straight-line), regardless of the distance to the pumping well,  
327 leading to equal estimated transmissivity or hydraulic conductivity values for each  
328 observation well. Only the intercept of the straight line with the time axis will differ because  
329 the anisotropy terms are only incorporated in the well-function (or within the log term for the  
330 Jacob's approximation). The analytical solutions used here start (Theis + two no-flow  
331 boundaries) or end (Hantush and dual porosity) with radial flow (straight-line on semi-log  
332 diagram), suggesting that in the scheme of an ideal anisotropic aquifer the hydraulic

333 conductivity estimates for a particular pumping test should be the same or very close between  
 334 wells. Such a statement is valid for the test performed at IFP30-4 in the horizontal stratiform  
 335 fissured granite far from the quartz reef, where observation wells are laid out at right angles  
 336 ( $K_{30-4} \approx K_{30-8} \approx K_{30-3} \approx 6.4 \times 10^{-6}$  m/s; Table 5). In addition, the estimated storativity for  
 337 the two observation wells is very close ( $7-8 \times 10^{-3}$ ), indicating an anisotropy ratio near 1 when  
 338 using the earlier mentioned anisotropic model. This suggests that at IFP30-4 the stratiform  
 339 horizontal fissured layer is neither affected by a significant anisotropy in hydraulic  
 340 conductivity onto the horizontal plane, nor affected by significant heterogeneities in hydraulic  
 341 conductivity at the pumping-test scale. However, this information should be confirmed by one  
 342 or more additional observation wells in other directions, or by additional tests in one of the  
 343 two observation wells (Neuman et al., 1984).

344

### 345 **3.3.2. Heterogeneous and anisotropic aquifer: verticalized fissured granite and quartz**

346 In the quartz reef (tests in IFP30-5 and IFP30-10) and in the granite at the pinch-out zone of  
 347 the reef (IFP1-6), the estimated hydraulic conductivity differs between wells with a factor  
 348 between 3 and 5 (Tables 3, 4 and 6). This implies that the tested aquifers are not ideal  
 349 anisotropic aquifers or/and are affected by significant heterogeneity in hydraulic conductivity  
 350 as illustrated by the analysis of slug-test data (Fig. 5).

351 Based on synthetic aquifers with heterogeneous transmissivity and homogeneous storativity,  
 352 Meier et al. (1998) and Sánchez-Vila et al. (1999) showed that for long-duration tests the  
 353 transmissivity values obtained with the Jacob straight-line method on observation wells at  
 354 various distances from the pumping well are almost identical to the average transmissivity of  
 355 the medium, even if the heterogeneity in transmissivity is important. However, storativity  
 356 estimates vary considerably which, according to these works, is a result of the heterogeneity  
 357 in transmissivity. Our aquifer hydraulic conductivity and storativity data set can be interpreted  
 358 similarly: the used methods provide representative hydraulic conductivity values of the  
 359 aquifers since K estimates are comparable, and the high variability in storativity estimates,  
 360 which can be about an order of magnitude for the same test, may be the consequence of a  
 361 heterogeneous hydraulic conductivity field. According to Meier et al. (1998) and Sánchez-  
 362 Vila et al. (1999), a well located in a high hydraulic-conductivity zone compared to the  
 363 estimated one, results in an overestimated storativity value, and vice versa. Furthermore, the  
 364 obtained transmissivity depends not only on the transmissivity values along the connecting  
 365 path, but also on the average transmissivity values of the full domain (Sánchez-Vila et al.,  
 366 1999). With our data set, no correlation between slug-test data and storativity was found,

367 probably because of the very local estimation assigned to this method (slug tests have an  
 368 action radius of a few metres around the well). Strong increases of the transmissivity  
 369 variability of these numerical models, which was introduced by increases in the variance  
 370 transmissivity fields, produced ellipsoidal shapes of estimated transmissivity around the  
 371 pumping well, which were even better defined when the highest transmissivity zones were  
 372 connected by highly permeable fractures. Even though these shapes may be exaggerated due  
 373 to numerical artefacts, they seem nevertheless related to the transmissivity field. This point  
 374 was, however, not discussed by the authors.

375

### 376 **3.3.3. Proposed methodology for identifying the major and minor axes in hydraulic** 377 **conductivity and results**

378 In order to understand the variations in hydraulic conductivity estimated from one well to  
 379 another, we prepared graphs representing the hydraulic conductivity values obtained at each  
 380 observation well on the X-Y plane (K values from Tables 3, 4 and 6). If hydraulic  
 381 conductivity estimates depend upon the hydraulic conductivity values along the connecting  
 382 path between the pumping well and the observation well as well as on the average hydraulic  
 383 conductivity value at the pumping test scale, one may expect variations in estimated values  
 384 according to the direction between the pumping well and the observation well.

385 The hydraulic conductivity estimated in a particular observation well ( $K_{obs.well}$ ) is plotted as  
 386 a function of the angle  $\beta$  between the geographical north (reference axis) and the pumping-  
 387 well / observation-well direction. Each  $K_{obs.well}$  is thus defined by two components,  $K_E$   
 388 representing the projection onto the east-west or X-axis ( $K_E = K_{obs.well} \times \cos\beta$ ) and  $K_N$ , the  
 389 projection onto the north-south or Y-axis ( $K_N = K_{obs.well} \times \sin\beta$ ). The pumping well is located  
 390 at the centre of the graph.

391 The three tests where the method was applied (Figs. 7a, b and c) clearly show correlations  
 392 between the estimated hydraulic conductivity and the orientation of the well to the pumping  
 393 well. Regardless of the distance between pumping well and observation well, the plotted  
 394 hydraulic conductivities describe ellipses showing that the hydraulic conductivities obtained  
 395 along the reef axis are systematically larger than the orthogonal estimates. Higher values are  
 396 explained by the velocity at which the drawdown propagates, which depends upon the  
 397 hydraulic diffusivity ( $D = K.b/S$ ;  $b$  being the aquifer thickness). Because the variability in  
 398 hydraulic conductivity is usually much larger than the storativity one, diffusivity is thus large  
 399 for highly conductive zones and small for low-conductivity zones. Thus, when pumping, a

400 vertical hydraulic gradient from lower to higher conductive zones is induced, which means  
 401 that the highly conductive fissures or the fissure network that is best connected to the  
 402 pumping well can be regarded as drainage structures or as lateral extensions of the well  
 403 (Schad and Teutsch, 1994).

404 Hydraulic conductivity ellipses are defined by major and minor axes ( $K_{max}$  and  $K_{min}$ ) and  
 405 are supposed to characterize an average pseudo or apparent anisotropy introduced by the  
 406 heterogeneity in hydraulic conductivity of the aquifer, or, in the case of fractured media, the  
 407 variability in hydraulic connectivity with the different well locations;  $\alpha$  representing the angle  
 408 between the Y-axis and  $K_{max}$ . The ratios  $K_{max}/K_{min}$  are comparable, between 2.6 and 3.1,  
 409 and reveal the degree to which the fissures in the two orthogonal orientations are connected;  
 410 however, the ratio values were not interpreted in a quantitative sense. To agree with previous  
 411 work - the evaluated hydraulic conductivity at the pumping well should be representative of  
 412 the whole heterogeneous medium (Meier et al., 1998) - but also to validate the analysis, the  
 413 hydraulic conductivity estimated for the pumping well should represent the average hydraulic  
 414 conductivity of the aquifer and should be close to the average hydraulic conductivity value  
 415 deduced from this analysis ( $K_{mean}=[K_{max} \cdot K_{min}]^{0.5}$ ). Using such an approach,  $K_{mean_{30-10}}=5.9$   
 416  $\times 10^{-6}$  m/s is compared to  $K_{IFP30-10}=6.3 \times 10^{-6}$  m/s,  $K_{mean_{30-5}}=3.6 \times 10^{-6}$  m/s to  $K_{IFP30-5}=4.2 \times$   
 417  $10^{-6}$  m/s, and  $K_{mean_{1-6}}=5.1 \times 10^{-6}$  m/s to  $K_{IFP1-6}=5.1 \times 10^{-6}$  m/s. Differences are thus small,  
 418 between 0 to 15%, compared to the ones obtained from pumping wells. However, the ellipses  
 419 are mismatched in a few points. Some lie outside the ellipse, such as IFP1-1, which suggests  
 420 that the pressure transfer is easier between this well and the pumping well due to a  
 421 preferential flow path as previously suggested, or they lie inside the ellipse due to a lower  
 422 conductive zone (IFP30-8, IF30-7; Fig. 7b).

423 From this analysis, it results that the major ellipse axes are clearly oriented sub-parallel to the  
 424 quartz reef. Consequently, for the tests in the quartz reef, it can be concluded that the sub-  
 425 vertical fissure set parallel to the reef axis ensures a preferential connection between the  
 426 pumped and the other wells. However, at right angles to the reef the connection is lower, most  
 427 probably because of the variation in the degree of fissuring between the heart and the side of  
 428 the reef.

429 In the verticalized fissured layer at the quartz vein pinch-out zone (Fig. 7c), we also find  
 430 variability in the connectivity of the fissure network. The major axis is also sub-parallel to the  
 431 sub-vertical fissure set and parallel to the reef axis. This result suggests that in the pinch-out  
 432 zone of the quartz reef, and probably also at the contacts on the eastern and western sides, the  
 433 verticalized fissured granite is affected by a dominant set of sub-vertical conductive fissures

434 sub-parallel to the reef. This feature differs from the classic stratiform horizontal fissured  
 435 layer, where horizontal conductive fissures dominate (Fig. 1; Maréchal et al., 2004).

436

437

## 438 **4. HYDROGEOLOGICAL CONCEPTUAL MODEL OF THE QUARTZ** 439 **REEF**

440 Geological, hydrogeological and geophysical investigations performed along the quartz reef  
 441 allow completing the understanding of the structure and the hydrogeological properties of  
 442 hard-rock aquifers exposed to deep weathering processes (Fig. 8).

443

### 444 **4.1. Aquifer geometry**

445 Near the quartz reef the weathering fronts within the granite (e.g. bottom of saprolite and of  
 446 the fissured layer) are noticeably deeper compared to the classic stratiform weathering profile.

447 On average, the thickness of the saprolite increases by a factor of 1.5 to 3 and that of the  
 448 fissured layer by a factor of 3 to 5. Near the contact, the geometry of the weathering profile in  
 449 the granite is, as for the classic stratiform weathering profile, characterized by two sub-  
 450 parallel layers: the saprolite and the fissured layers. However, they are not sub-parallel to the  
 451 paleo-surface contemporaneous with the weathering, but sub-parallel to the discontinuity  
 452 borders. As a result, the weathering profile exhibits a ‘U’ shape composed of parallel layers.

453 The quartz reef is characterized by mainly sub-vertical fissures that are sub-parallel and sub-  
 454 orthogonal to the reef axis. The top layer is highly fissured and weathered and the fissure  
 455 density rapidly decreases with depth. Density in fissuring and the grade of weathering vary  
 456 also in space and are more pronounced at the contact with granite, i.e. on the sides and in the  
 457 pinch-out zones, than at the heart of the vein. This ‘U’ shape of the weathering layers results  
 458 from similar processes as those observed in horizontal stratiform weathering profiles:

- 459 (i) The constraints resulting from the development of the weathering profile in the granite  
 460 surrounding the quartz reef induce fissuring of the quartz reef. This explains the  
 461 numerous metre- to decametre-wide fissures observed in the quartz reef outcrops.  
 462 Constraints in the granite are induced by the swelling of some minerals, particularly  
 463 biotite (Wyns et al., 1999, 2004; Lachassagne et al., 2011);
- 464 (ii) This weathering-induced fissuring enhances water circulation and in return favours a  
 465 local deepening of the weathering fronts in the granite near the contact with the quartz  
 466 reef. The lower strain is thus deviated in the direction of the discontinuity, which favours

467 the development of a verticalized fissured layer in the granite at the contact with the reef.  
 468 This point is supported by the heterogeneity in hydraulic conductivity, which shows  
 469 evidence that this layer is characterized by dominant conductive fissures sub-parallel to  
 470 the intrusion

471 (iii) The induced weathering favours deeper fissures in the quartz vein, and so on.

472 Thus, during the weathering of granitic formations such a discontinuity favours a local  
 473 deepening of the weathering fronts in the host rock and thus favours a thickening of the  
 474 transmissive part of the aquifer (the fissured layer). In addition, the quartz vein is also subject  
 475 to weathering. It causes small-scale fissures that further enhance the hydraulic conductivity.  
 476 This *in situ* weathering amplifies the above-described process.

477 Intrusives or veins whose weathering products are of low permeability, such as those of  
 478 dolerite dykes, do not favour water circulation, neither in their heart, nor around them. The  
 479 stratiform weathering profile of the neighbouring granite thus remains undisturbed. Moreover,  
 480 such dykes —as in the case of the IFP1 site— act as low-permeability barriers that  
 481 compartment the horizontal fissured layer.

482

## 483 **4.2. Hydrodynamic properties of the aquifer**

### 484 ***4.2.1. Granite near the contact with the discontinuity***

485 Far from the quartz reef, the stratiform horizontal fissured layer of the granite is characterized  
 486 by quite homogenous hydrodynamic parameters (pumping tests in IFP1-8 and IFP30-4): the  
 487 hydraulic conductivity is about  $10^{-5}$  m/s and the storativity ranges between 0.2 and  $7 \times 10^{-3}$ .  
 488 These values are similar to the ones found in the same area:  $K=5 \times 10^{-5}$  m/s and  $S=6 \times 10^{-3}$ ,  
 489 (Maréchal et al., 2004), and  $K=1.6 \times 10^{-5}$  m/s (Dewandel et al., 2006). As previously shown  
 490 by Maréchal et al. (2004), the granite is characterized by dual-porosity behaviour, being  
 491 affected by sub-horizontal and sub-vertical fissure networks and low-permeability blocks with  
 492 a hydraulic conductivity of about  $3 \times 10^{-9}$  m/s. In addition, the two fissure sets induce a  
 493 significant horizontal anisotropy in permeability ( $K_{\text{horiz.}}/K_{\text{vert.}}$ : 10) because of the well-  
 494 developed horizontal conductive fissure network. The pumping test performed in IFP1-8  
 495 within the horizontal fissured layer did not show such behaviour as a result of the presence of  
 496 the low-permeability dolerite dyke which became apparent at the early stage of the pumping  
 497 and masked the dual-porosity behaviour.

498 The average hydraulic conductivity of the verticalized fissured layer along the quartz reef is  
 499 about  $4.5 \times 10^{-6}$  m/s, and the average storage coefficient  $7.8 \times 10^{-4}$  (-). The similarity between  
 500 these values and the ones from the ‘classic’ stratiform horizontal fissured layer in the area

501 suggests that the conductive zones of both horizontal and verticalized fissured layers have a  
 502 similar origin, i.e. weathering processes. As in the case of the IFP1-8 test, the two no-flow-  
 503 boundaries that appear at the early stage of pumping in IFP1-6 probably masked the dual-  
 504 porosity behaviour of the verticalized granite. However, this layer may also behave like such  
 505 a medium, as suggested by the low local hydraulic-conductivity values derived from slug  
 506 tests, 1 to  $4 \times 10^{-7}$  m/s (IFP30-3 and IFP1-3), which are typical of the hydraulic conductivity  
 507 values in the block as given by Maréchal et al. (2004). Thus, the verticalized fissured layer of  
 508 the granite along the contact with the reef is formed by a conductive fissure network ( $4.5 \times 10^{-6}$   
 509 m/s) and possibly by low-permeability blocks (about  $10^{-7}$  m/s). In addition, this verticalized  
 510 layer is characterized by a dominant set of conductive fissures that are sub-vertical and sub-  
 511 parallel to the reef axis ( $K_y > K_x$ ). This result differs from the ‘classic’ horizontal fissured  
 512 layer, where no significant anisotropy was found in the horizontal plane ( $K_x \approx K_y$  at IFP30-4)  
 513 and where a conductive sub-horizontal fissure network dominates ( $K_x/K_z=10$ ; Maréchal et al.,  
 514 2004).

#### 516 **4.2.2. Quartz aquifer**

517 The fissured quartz is characterized by a dual-porosity behaviour; the average hydraulic  
 518 conductivity of the fissure network is 4 to  $6 \times 10^{-6}$  m/s, storativity being 3 to  $5 \times 10^{-4}$  and  
 519 mainly ensured by low-permeability blocks ( $2.4 \times 10^{-9}$  m/s). However, hydrodynamic  
 520 properties in the quartz are highly variable in space and closely depend upon the grade of  
 521 weathering and fissuring: it is poorly fissured with low permeability in the heart and highly  
 522 conductive at the contact with granite due to an enhanced fissuring. The fissured quartz is also  
 523 characterized by anisotropy onto the vertical plane,  $K_x/K_z$ : 3, which is attributed to a  
 524 decreasing density with depth of the conductive fissures. As for the verticalized fissured layer  
 525 of the granite, conductive fissures that are sub-vertical and sub-parallel to the reef dominate in  
 526 the quartz, inducing a higher hydraulic conductivity parallel to the reef ( $K_y > K_x$ ); however,  
 527 the anisotropy in hydraulic conductivity could not be estimated.

528 Even if at Kothur site the aquifer also has a ‘U’ shape, hydraulic tests do not show evidence  
 529 of channelized groundwater flow. This is explained by the fact that during the tests the  
 530 groundwater level was very shallow (4 to 5 m deep) whereas it was more than 15 m deep at  
 531 the IFP1 site. As a consequence, at Kothur the ‘U’-shape aquifer was still well-connected to  
 532 the surrounding horizontal stratiform fissured layer of the granite aquifer, giving the  
 533 impression of an infinite aquifer while at the IFP1 site only the ‘U’ shape aquifer contributed  
 534 to pumping.

535

## 536 **5. CONCLUSIONS**

537 The obtained results complement the conceptual hydrogeological model developed for granite  
538 aquifers (Taylor and Howard, 2000; Maréchal et al., 2004; Dewandel et al., 2006) in places  
539 where geological discontinuities disturb the weathering profile.

540 Near the quartz reef, weathering processes appear to be at the origin of an enhanced local  
541 hydraulic conductivity both in the vein and in the surrounding granite. The quartz reef and the  
542 accompanying verticalized fissured granite layer at the contact constitute a composite aquifer  
543 characterized by a ‘U’-shaped geometry that acts as a local drain. This higher permeability is  
544 probably at the origin of the sharp deepening of the weathering front in the surrounding  
545 granite and in the quartz reef itself. Hydrodynamic properties of the verticalized fissured  
546 granite are comparable to those found in the classic horizontal fissured layer. However, the  
547 anisotropy in hydraulic conductivity is reversed as sub-vertical fissures control the  
548 groundwater flow at the discontinuity, while fluxes in the classic horizontal fissured layer are  
549 mostly controlled by a dominant set of sub-horizontal fissures.

550 Where the weathering can propagate downward, other geological discontinuities such as deep  
551 fractures, leucocratic dykes, pegmatite, or contacts between different geological formations,  
552 may also constitute local structures with similar aquifer properties as those described here. As  
553 a result, the weathering front should also form a ‘U’ shape depending upon how vertical the  
554 discontinuity is and on the duration of the weathering processes. Such types of structures,  
555 searched for and observed by hydrogeologists and geophysicists for borehole siting (e.g.  
556 Sander, 2007) are commonly attributed to “tectonic fracturing” (“fault gouges”). The novelty  
557 here is to show that the geometry of the aquifer and its hydrodynamic properties are inherited  
558 from deep and local *in situ* weathering processes, but are unrelated to tectonic activity.  
559 Therefore, where this deepening of the weathering front has developed such structures may be  
560 valuable targets for borehole siting, particularly because of the enhanced transmissivity due to  
561 an increase in aquifer thickness. However, the permeability of such structures is highly  
562 variable in space, being low in the heart and high at the contacts. Such contrasting  
563 hydrodynamic properties, and also the more or less important development of the weathering  
564 profile along these structures, may explain the high variability of well yields using a standard  
565 approach based only on the study of lineaments. Thus, lineament studies combined with  
566 structural studies of the weathering profile would improve the chances of siting productive  
567 wells. At the opposite, discontinuities that produce weathering material of low permeability,

568 such as dolerite dykes, do not locally enhance the thickness of weathered layers in granite or  
569 its hydraulic conductivity, making such structures unfavourable targets.  
570 Numerical issues, both for modelling the evolution of the weathering profile along such  
571 discontinuities and for modelling of the tests, as well as additional hydraulic tests to assess  
572 preferential flow paths (flowmeter tests), to pursue the quantification of heterogeneity in  
573 hydrodynamic properties in relation to underground reality (fissures orientation, structure of  
574 the weathered layers), are topics of interest for future research. In addition, the development  
575 of new analytical solutions for the interpretation of pumping tests in such media would help in  
576 improving their characterization, such as including anisotropy, channelized flow and/or the  
577 influence of surrounding aquifers.  
578 Finally, because of the complex structures and associated properties of such aquifers, special  
579 attention has to be paid to water management. The channelized or fractionalized patterns of  
580 the flow paths have strong implications in terms of contaminant transport and for delineating  
581 appropriate protection perimeters for water-supply wells. Efforts should thus be made for  
582 improving the hydrogeological and hydrogeochemical characterization of these aquifers to  
583 ensure their safe and sustainable groundwater exploitation. The methods for characterizing the  
584 aquifer used here could be used and improved for achieving this goal.

585

## 586 **Acknowledgements**

587 The authors are grateful to the research-sponsorship from BRGM (France), the Embassy of  
588 France in India, NGRI (India) and from the French National Research Agency (ANR) under  
589 the VMCS2008 program (SHIVA project n°ANR-08-VULN-010-01). Colleagues from NGRI  
590 and BRGM are thanked for their fruitful comments, discussions and technical assistance in  
591 the field. The three anonymous Journal referees are thanked for their useful remarks and  
592 comments that improved the quality of the paper. We are grateful to Dr. H.M. Kluijver for  
593 revising the English text.

594

595 **References**

- 596 Ayraud, V., Aquilina, L., ; Labasque, T., Pauwels, H., Molenat, J., Pierson-Wickmann,  
597 A.C., Durand, V., Bour, O., Tarits, C., Le Corre, P., Fourre, E., Merot, Pj. and Ph.  
598 Davy, 2008. Compartmentalization of physical and chemical properties in hard-rock  
599 aquifers deduced from chemical and groundwater age analyses. *Applied*  
600 *Geochemistry*, 2008, vol. 23 (9), 2686-2707.
- 601 Black, J.H. 1994. Hydrogeology of fractured rocks – a question of uncertainty about  
602 geometry, *Applied Hydrogeology*, 3, 56-70.
- 603 Blomqvist, R.G. 1990. Deep groundwater in the cristalline basement in Finland, with  
604 implications for waste disposal studies. *Geologiska Foereningen i Stockholm*  
605 *Foerhandlingar*, vol.112(4), pp.369-374.
- 606 Bourdet, D., Whittle T.M., Dougals, A.A. and Y.M. Pirard. 1983. A new set of type curves  
607 simplifies well test analysis, *World Oil*.
- 608 Bourdet D., Ayoud J.A. and Y.M. Pirard. 1989. Use of pressure derivative in well-test  
609 interpretation. *SPE*, 293-302.
- 610 Bouwer, H. and Rice R.C. 1976. A slug test for determining hydraulic conductivity of  
611 unconfined aquifers with completely or partially penetrating wells. *Water Resources*  
612 *Research*, 12, 3, 423-428.
- 613 Chandra, S., Rao, V.A., Krishnamurthy, N.S., Dutta S., and Ahmed, S., 2006. Integrated  
614 studies for characterization of lineaments to locate groundwater potential zones in  
615 hard rock region of Karnataka, India. *Hydrogeology Journal*, 14(5), 767-776.
- 616 Chandra S., Dewandel B., Kumar D., Dutta S. Bhat A.N., Murthy N.S.K. and S. Ahmed.  
617 2010. Geophysical Characterization of Quartz Reef Intrusive Lineaments in Granite  
618 Hard Rock for Groundwater Occurrences, *Applied Geophysics*, in press.
- 619 Chilton, P.J., and Foster, S.S.D. 1995. Hydrogeological characterization and water-supply  
620 potential of basement aquifers in tropical Africa. *Hydrogeology J.*, 3(1), 36-49.
- 621 Chilton, P.J. and Smith-Carrington, A.K. 1984. Characteristics of the weathered basement  
622 aquifer in Malawi in relation to rural water supplies. *Challenges in African Hydrology*  
623 *and Water Resources*, proc. Harare Symposium, July 1984, pp.57-72.
- 624 Cho M., K-M. Ha, Y-S. Choi, W-S. Kee, P. Lachassagne and R. Wyns. 2003. Relationship  
625 between the permeability of hard-rock aquifers and their weathered cover based on  
626 geological and hydrogeological observation in South Korea. IAH Conference on  
627 "Groundwater in fractured rocks", Prague 15-19 September 2003, Prague.

- 628 Courtois, N., Lachassagne, P., Wyns, R., Blanchin, R., Bougaïré, F.D., Somé, S. and A.  
 629 Tapsoba. 2010. Country-scale hydrogeological mapping of hard-rock aquifers and its  
 630 application to Burkina Faso, *Ground Water*, in press.
- 631 Dewandel B., Lachassagne P., R.Wyns, Maréchal J.C. and N.S. Krishnamurthy, 2006. A  
 632 generalized hydrogeological conceptual model of granite aquifers controlled by single  
 633 or multiphase weathering. *Journal of Hydrology*, 330, 260-284,  
 634 doi:10.1016/j.jhydrol.2006.03.026.
- 635 Dewandel, B., Perrin, J., Ahmed, S., Aulong. S., Hrkal, Z., Lachassagne, P., Samad, M., S.  
 636 Massuel. and A. Mukherji. 2008. Management of the groundwater resources in semi-  
 637 arid hard rock regions under variable water demand and climatic conditions:  
 638 development of a Decision Support Tool. Groundwater & Climate in Africa  
 639 International Conference, Kampala, Uganda June 24-28.
- 640 Dewandel, B., Perrin, J., Ahmed, S., Aulong. S., Hrkal, Z., Lachassagne, P., Samad, M. and  
 641 S. Massuel. 2010. Development of a Tool for managing groundwater resources in  
 642 semi-arid hard rock regions. Application to a rural watershed in South India.  
 643 *Hydrological Processes*, in press.
- 644 Ehlig-Economides, C.A. 1988. Use of the Pressure Derivative for Diagnosing Pressure-  
 645 Transient Behavior, *Journ. of Petroleum Technology*, oct.1988.
- 646 G.I.S., 2002. Geological Survey of India. Geological map: Hyderabad quadrangle – Andhra  
 647 Pradesh.
- 648 Gustafson, G. and J. Krásný. 1994. Crystalline rock aquifers: their occurrence, use and  
 649 importance, *Applied Hydrogeology*, 2, 64-75.
- 650 Hantush, M.S. 1961. Aquifer tests on partially penetrating wells. *Proc. of the Am. Soc. of*  
 651 *Civil Engineers*, 87, 171-195.
- 652 Hantush M.S. 1966. Analysis of data from pumping tests in anisotropic aquifers. J.  
 653 *Geophys. Res.*, 72, 1709-1720.
- 654 Hantush M.S. and R.G. Thomas. 1966. A method for analyzing a drawdown test in  
 655 anisotropic aquifer. *Trans. Am. Geophys. Union*, 36, 281-285.
- 656 Houston, J.F.T., and R.T. Lewis. 1988. The Victoria Province drought relief project, II.  
 657 Borehole yield relationships. *Ground Water*, 26(4), 418-426.

- 658 Howard, K.W.F., M. Hughes, D.L. Charlesworth, and G. Ngobi. 1992. Hydrogeologic  
 659 evaluation of fracture permeability in crystalline basement aquifers of Uganda.  
 660 *Applied Hydrogeology*, 1, 55-65.
- 661 Jacob, C.E., 1947. Drawdown test to determine effective radius of an artesian well, *ASCE*  
 662 *Trans.*, 112(232), 1047-1064.
- 663 Krásný J. and J. Sharp, 2007. Hydrogeology of fractured rocks from particular fractures to  
 664 regional approaches : state-of-the-art and future challenge. In: Krásný J. – Sharp J.M.  
 665 (eds.): *Groundwater in fractured rocks, IAH Selected Papers*, 9, 1-30. Taylor and  
 666 Francis.
- 667 Kuusela-Lahtinen, A., Niemi, A. and Luukkonen, A. 2003. Flow dimension as an indicator  
 668 of hydraulic behaviour in site characterization of fractured rock. *Ground Water*,  
 669 vol. 41 (3), pp.33-341.
- 670 Lachassagne, P., B. Dewandel B., R. Wyns. 2011. The fracture permeability of Hard Rock  
 671 Aquifers is due neither to tectonics, nor to unloading, but to weathering processes.  
 672 *Terra Nova*, 23, 145-161.
- 673 Lachassagne, P., R. Wyns, P. Bérard, T. Bruel, L. Chéry, T. Coutand, J.F. Desprats, and P.  
 674 Le Strat. 2001. Exploitation of high-yield in hard-rock aquifers: Downscaling  
 675 methodology combining GIS and multicriteria analysis to delineate field prospecting  
 676 zones. *Ground Water*, 39(4), 568-581.
- 677 Le Borgne, Bour, O., de Dreuzy J.R., Davy, P. and F. Touchard. 2004. Equivalent mean  
 678 flow models for fractured aquifers: insights from a pumping tests scaling  
 679 interpretation. *Water Res. Research*, 40, W03512, 1-12.
- 680 Le Borgne, Bour, O., Paillet F.L and J-P. Caudal. 2006. Assessment of preferential flow  
 681 path connectivity and hydraulic properties at single-borehole and cross-borehole  
 682 scales in fractured aquifer. *J. of Hydrology*, 328, 347-359.
- 683 Leveinen, J., E. Rönkä, J. Tikkanen and E. Karro. 1998. Fractional flow dimensions and  
 684 hydraulic properties of a fracture-zone aquifer, Leppävirta, Finland. *Hydrogeology J.*,  
 685 vol.6, 327-340.
- 686 Lods, G. and Ph. Gouze. 2004. WTFM, software for Well Test analysis in Fractured Media  
 687 combining fractional flow with double porosity and leakance approaches. *Computer &*  
 688 *Geosciences Journal*. 937-947.

- 689 Loke M.H., Barker R.D., 1996. Rapid least-squares inversion of apparent resistivity  
690 pseudosections using a quasi-Newton method. *Geophysical Prospecting*, 44, 131-152.
- 691 Mabee, S.B., Hardcastle, K.C. and Wise, D.U., 1994. A method of collecting and analyzing  
692 lineaments for regional scale fissured-bedrock aquifer studies. *Ground Water*, 32(4),  
693 pp.884-894.
- 694 Maréchal J.C., B. Dewandel, and K. Subrahmanyam. 2004. Use of hydraulic tests at  
695 different scales to characterize fracture network properties in the weathered-fissured  
696 layer of a hard rock aquifers. *Water Resources Res.*, vol.40, W11508.
- 697 Maréchal, J.C., B. Dewandel, S. Ahmed, L. Galeazzi, 2006. Combining the groundwater  
698 budget and water table fluctuation methods to estimate specific yield and natural  
699 recharge. *Journal of Hydrology*, 329, 1-2, 281-293, doi:10.1016/j.jhydrol.2006.02.022.
- 700 Maréchal, J.-C., Dewandel, B., Ahmed S. and P. Lachassagne, 2007. Hard-rock aquifers  
701 characterization prior to modelling at catchment scale: an application to India. In:  
702 Krásný J. – Sharp J.M. (eds.): *Groundwater in fractured rocks, IAH Selected Papers*,  
703 9, 1-30. Taylor and Francis.
- 704 Meier, P.M., Carrera, J., and X. Sánchez-Vila, 1998. An evaluation of Jacob's method for  
705 the interpretation of pumping tests in heterogeneous formations. *Water Resources*  
706 *Research*, 34 (5), 1011-1025.
- 707 Nahon, D. B. 1991. Introduction to the Petrology of Soils and Chemical Weathering. Ed.  
708 Wiley.
- 709 Neuman, S.P., Walter G.R., Bentley H.W., Ward J.J. and D.D. Gonzalez. 1984.  
710 Determination of horizontal aquifer anisotropy with three wells. *Ground Water*, 22-1,  
711 66-72.
- 712 Omorinbola, E.O. 1982. Verification of some geomorphological implications of deep  
713 weathering in the basement complex of Nigeria. *Journal of Hydrology*, 56, 347-368.
- 714 Owoade, A. 1995. The potential for minimizing drawdowns in groundwater wells in tropical  
715 aquifers. *Journ. of African Earth Sciences*, 20, 3-4, 289-293.
- 716 Pickens, J.F., Grisak, G.E., Avis, J.D., Belanger, D.W. and Thury, M. 1987. Analysis and  
717 interpretation of borehole hydraulic tests in deep boreholes; principles model  
718 development, and applications. *Water Resources Res.*, vol. 23(7), pp.1341-1375.
- 719 Ramey, H.J. 1975. Interference analysis for anisotropic formations – a case history. *Jour. of*  
720 *Petroleum Technology.*, 1290-1298.

- 721 Renard, Ph., Glenz D. and M. Mejias. 2009. Understanding diagnostic plots for well-test  
722 interpretation. *Hydrogeology Journal*, 17, 589-600.
- 723 Sánchez-Vila, X., Meier, P.M. and J. Carrera, 1999. Pumping tests in heterogeneous  
724 aquifers: an analytical study of what can be obtained from their interpretation using  
725 Jacob's method. *Water Resources Research*. 35 (4), 943-952.
- 726 Sander P, Minor TB, Chesley M.M. 1997. Groundwater exploration based on lineament  
727 analysis and reproducibility tests. *Ground Water* 35(5):888–894.
- 728 Sander P. 2007. Lineaments in groundwater exploration: a review of applications and  
729 limitations.- *Hydrogeology Journal*, 15(1), 71-74.
- 730 Schad, H. and G. Teutsch, 1994. Effects of the investigation scale on pumping test results in  
731 heterogeneous porous aquifers. *Journal of Hydrology*, 159, 61-77.
- 732 Spane F.A. and Wurstner S.K., 1993. DERIV: a computer program for calculating pressures  
733 derivatives for use in hydraulic test analysis. *Ground Water* 31:814–822.
- 734 Tardy, Y., 1971. Characterization of the principal weathering types by the geochemistry of  
735 waters from some European and African crystalline massifs. *Chemical Geology*, vol.7,  
736 253-271.
- 737 Tardy, Y. 1993. *Pétrologie des latérites et des sols tropicaux*.- 459 pp.- Masson, Paris.
- 738 Tardy, Y. 1998. *Dérive des continents, latérites et paléoclimats tropicaux*.- 472 pp.-  
739 Editions BRGM, Orléans.
- 740 Taylor, R., and K. Howard. 2000. A tectono-geomorphic model of the hydrogeology of  
741 deeply weathered crystalline rock: evidence from Uganda. *Hydrogeology J.*, 8(3), 279-  
742 294.
- 743 Uhl, V.W. and G.K. Sharma. 1978. Results of pumping tests in crystalline-rock aquifers.  
744 *Ground Water*, vol.16 (3), pp. 192-203.
- 745 Walker, D.D., Gylling, B., Strom, A. and J.O. Selroos. 2001. Hydrogeologic studies for  
746 nuclear-waste disposal in Sweden. *Hydrogeology J.*, vol.9(5), pp.419-431.
- 747 Wyns, R., J.-C. Gourry, J.-M. Baltassat, and F. Lebert. 1999. Caractérisation  
748 multiparamètres des horizons de subsurface (0-100 m) en contexte de socle altéré, in  
749 *2ème Colloque GEOFCAN*, edited by BRGM, IRD, UPMC, pp. 105-110, Orléans,  
750 France.

751 Wyns, R., J. M. Baltassat, P. Lachassagne, A. Legchenko, J. Vairon, and F. Mathieu. 2004.  
752 Application of SNMR soundings for groundwater reserves mapping in weathered  
753 basement rocks (Brittany, France), *Bulletin de la Société Géologique de France*, 175  
754 (1), pp. 21-34.  
755

756 **Figure captions**

757

758 Figure 1. Idealized weathering profile in hard-rock intersected by the current topography. The  
759 insert presents the area of interest of the paper: geological discontinuities (Wyns et al., 1999).

760

761 Figure 2. Location of the studied area with main geological features (G.S.I., 2002);  
762 Maheshwaram area, Ranga Reddy District, Andhra Pradesh, India.

763

764 Figure 3. Geological information and borehole locations. (a) IFP1 and (b) Kothur pilot sites.  
765 Lines A, B and C materialize the cross sections (see Figs. 6), and the other dotted lines the  
766 location of electrical-resistivity profiles (identical to line A for IFP1 site). Grey curves: soil  
767 elevation (masl). BW: farmer's wells.

768

769 Figure 4. Interpreted geological cross sections. (a) perpendicular to the quartz reef at IFP1  
770 site, (b) perpendicular and (c) parallel to the quartz reef at Kothur site. Location of the cross  
771 sections is shown on Figure 3 (lines A, B and C).

772

773 Figure 5. Histogram on a logarithmic scale of the hydraulic conductivity deduced from slug  
774 tests analysis. The data from the boreholes located in the quartz reef (average:  $\text{LogK}: -5.58$   
775  $\pm 1.0$ ; number of data [n]: 6) and in the granite surrounding the reef (average:  $\text{LogK}: -5.62$   
776  $\pm 0.6$ ; n: 15) are compared to the granite far from discontinuities (average:  $\text{LogK}: -5.36 \pm 1.0$ ,  
777 n: 30; Maheshwaram area [same area] Maréchal et al., 2004). LogK: natural logarithm of  
778 hydraulic conductivity.

779

780 Figure 6. Observed and modelled drawdowns and derivatives. (a) Pumping well IFP30-5 and  
781 observation well IFP30-2; model: Hantush (WinIsape software). (b) Pumping well IFP30-10,  
782 and observation wells IFP30-5 and IFP30-.6; model: dual porosity. IFP 30-6 considers the  
783 response of the matrix (WTFM software) (c) Pumping well IFP1-6 and observation well  
784 IFP1-9; model: Theis+2 no-flow boundaries (WinIsape software).

785

786 Figure 7. Heterogeneity in hydraulic conductivity on the horizontal plane. (a) Pumping at  
787 IFP30-5; hydraulic conductivity from Table 3. (b) Pumping at IFP30-10; hydraulic  
788 conductivity from Table 4. (c) Pumping at IFP1-6; hydraulic conductivity from Table 6.

789 Circles: wells located in the quartz reef; triangles: wells located in the granite. Error bars  
 790 depict the range of the estimates deduced from the drawdown curve interpretations.  $\alpha$ : angle  
 791 between  $K_y$  and  $K_{max}$ .

792

793 Figure 8. Idealized conceptual hydrodynamic model of the aquifer associated to the quartz  
 794 reef. Data from the horizontal stratiform fissured layer are from Maréchal et al. (2004) and  
 795 Dewandel et al. (2006).

796

797

## 798 Table captions

799

800 Table 1. Characteristics of the wells in the IFP1 and Kothur sites and hydraulic conductivity  
 801 (K) deduced from slug tests.

802

803 Table 2. Characteristics of pumping tests performed at the IFP1 and Kothur pilot sites.  
 804 \* Geology of the aquifer zone; \*\* drawdown at the end of pumping, and \*\*\* number of  
 805 observation wells that reacted to pumping. The diagnoses are deduced from derivative curve  
 806 analyses.

807

808 Table 3. Results of the interpretation of the pumping in IFP30-5 (Kothur site; quartz aquifer).  
 809 Model: Hantush (partially penetrating well). \* drawdown at the end of pumping, \*\* K and S  
 810 are geometrical mean; others are arithmetic mean, and \*\*\* estimated from geological logs.  
 811 StDev.: standard deviation.

812

813 Table 4. Results of the interpretation of pumping in IFP30-10 (Kothur site; quartz aquifer).  
 814 Model: dual-porosity. \* observation well interpreted in the matrix, \*\* drawdown at the end of  
 815 pumping, and \*\*\* geometrical mean.

816

817 Table 5. Results of the interpretation of the pumping in IFP30-4 (Kothur site; granite aquifer).  
 818 Model: dual-porosity. \* drawdown at the end of pumping, and \*\* geometrical mean.

819

820 Table 6. Results of the interpretations of pumping in IFP1-6 (IFP1 site; granite aquifer).

821 Model: Theis + two no-flow boundaries. \* drawdown at the end of pumping, \*\* estimated

822 using the average S (7.8E-4), \*\*\* the number between comas is estimated using the average S  
823 and \*\*\*\* K and S are geometrical mean, do not include data from observation wells IFP 1-3,  
824 1-4 and 1-8 (located in another aquifer); distances to limits are arithmetic mean.  
825  
826

827  
828  
829

**Tables**

Well ID	site	Depth (m)	Casing depth (m)	Main Geology	Saprolite thickness -granite (m)	Highly weathered quartz (m)	Basement depth (m)	K_slug (m/s)
IFP1	IFP1	42.0	8.8	Granite	18.3	-	37.5	7.4E-06
IFP1-1	IFP1	59.5	5.8	Granite	15.5	-	51	3.2E-06
IFP1-2	IFP1	35.0	12	Granite	22.5	-	30.2	7.4E-06
IFP1-3	IFP1	35.0	5.7	Granite	17	-	29	4.4E-07
IFP1-4	IFP1	68.6	6	Dolerite+granite	no data	-	77.7	7.6E-07
IFP1-5	IFP1	73.2	11.6	Granite		9	32	2.9E-06
IFP1-6	IFP1	73.2	22.9	Granite	13.5	2.5 (overlying the saprolite)	51	3.1E-06
IFP1-7	IFP1	59.4	27.1	Granite	11.5		44	3.9E-06
IFP1-8	IFP1	54.9	11.6	Dolerite+granite	7 m of highly weathered dolerite (clay)		41	6.5E-06
IFP1-9	IFP1	59.4	18.3	Granite	12.8		49	6.0E-06
IFP30-1	Kothur	91.4	11.6	Quartz		6.5	91.4	5.6E-07
IFP30-2	Kothur	45.7	29.9	Granite	20.6	4.0 (overlying saprolite)	41	2.8E-06
IFP30-3	Kothur	50.3	29.9	Granite	27.1	2.7 (overlying saprolite)	36.5	8.5E-08
IFP30-4	Kothur	50.3	29.9	Granite	29.2		42	8.8E-06
IFP30-5	Kothur	77.7	17.4	Quartz		20.2	77.7	5.1E-06
IFP30-6	Kothur	50.3	11.6	Quartz		6.8	50.3	5.1E-08
IFP30-7	Kothur	64.0	30.2	Granite	16.7	8.8 (overlying saprolite)	51.5	4.5E-07
IFP30-8	Kothur	50.0	42.7	Granite	28		38	6.3E-06
IFP30-9	Kothur	59.4	30.5	Quartz		39.5	50	1.1E-05
IFP30-10	Kothur	73.0	27.4	Quartz		30	73	1.6E-05
IFP30-11	Kothur	74.0	12.2	Quartz		25.5	36.5	1.30E-05

830  
831  
832  
833

Table 1.

Pumping Wells	Tested aquifer *	Well radius (m)	Pumping rate (m <sup>3</sup> /h)	Duration of the test (min.)	Max. dd. (m)**	Nb. of obs. wells ***	Diagnosis
IFP1-6	granite	0.11	13.5	1580	21.48	9	Channelized flow
IFP1-8	granite	0.11	3.5	1430	5.51	3	One-no flow boundary
IFP30-4	granite	0.11	6.8	1440	10.31	2	Dual porosity
IFP30-5	quartz	0.11	4.9	1440	8.33	7	Partially penetrating well
IFP30-10	quartz	0.11	16.3	2890	9.9	8	Dual porosity

834  
835  
836  
837  
838  
839  
840  
841  
842

Table 2.

843

Well ID		r (m)	s-max* (m)	K (m/s)	S (-)	Anisotropy Kx/Kz (-)	Aquifer thickness (m)	Screened thickness (m)***
IFP30-5	pump. well	0.11	8.33	4.2E-06	-	3.1	110	35
IFP30-1	obs.well	30.1	1.12	3.6E-06	1.4E-03	3.5	140	10
IFP30-2	obs.well	27.3	2.13	2.6E-06	4.0E-04	2.0	130	40
IFP30-6	obs.well	96.2	0.44	3.4E-06	1.8E-03	3.0	130	20
IFP30-7	obs.well	52.5	0.45	2.9E-06	7.5E-03	10.0	110	50
IFP30-9	obs.well	88.0	1.18	5.1E-06	4.5E-05	1.0	100	100
IFP30-10	obs.well	135.5	1.06	5.5E-06	2.7E-05	1.0	100	100
IFP30-11	obs.well	180.6	0.85	5.9E-06	3.5E-05	1.0	100	100
IFP30-3	obs.well	62.5	No reaction	-	-	-	-	-
IFP30-4	obs.well	103.0	No reaction	-	-	-	-	-
IFP30-8	obs.well	118.0	No reaction	-	-	-	-	-
Average**				4.0E-06	3.2E-04	3.1	115.0	
Std.Dev (±)				1.2E-06	2.7E-03	3.0	16.0	

844

845

Table 3.

846

847

Well		r (m)	s-max** (m)	Kf (m/s)	Km (m/s)	Sf (-)	Sm (-)	Stot (-)
IFP30/10	pump. well	0.11	9.9	6.3E-06	2.4E-09	-	-	-
IFP30/1	obs.well	123.2	3.38	8.5E-06	4.5E-10	4.9E-05	6.1E-05	1.1E-04
IFP30/2	obs.well	115.1	3.63	6.5E-06	1.9E-09	4.2E-05	1.8E-04	2.2E-04
IFP30/5	obs.well	135.7	4.42	6.5E-06	6.0E-10	1.5E-05	4.9E-05	6.4E-05
IFP30/6*	obs.well	222.0	1.27	1.1E-05	1.5E-09	8.5E-05	1.3E-04	2.1E-04
IFP30/7*	obs.well	145.0	1.04	6.0E-06	8.0E-09	2.4E-04	2.2E-03	2.5E-03
IFP30/8	obs.well	92.0	0.18	2.1E-06	2.6E-08	4.9E-03	6.1E-02	6.6E-02
IFP30/9	obs.well	49.4	5.5	6.5E-06	1.4E-09	2.6E-05	1.2E-04	1.5E-04
IFP30/11	obs.well	57.8	4.97	6.2E-06	5.5E-09	5.2E-05	1.9E-04	2.4E-04
IFP30/3	obs.well	132.8	No reaction	-	-	-	-	-
IFP30/4	obs.well	144.5	No reaction	-	-	-	-	-
geomean***				6.2E-06	2.4E-09	8.9E-05	3.5E-04	4.6E-04
StDev (±)				2.4E-06	8.2E-09	1.7E-03	2.1E-02	2.3E-02

848

849

Table 4.

850

851

852

Well	WTFM	r (m)	s-max* (m)	Kf (m/s)	Km (m/s)	Sf (-)	Sm (-)	Stot (-)
IFP30/4	pump. well	0.11	10.31	6.4E-06	4.0E-09	-	-	-
IFP30/3	obs.well	40.6	1.08	6.5E-06	7.0E-09	9.5E-05	6.7E-03	6.8E-03
IFP30/8	obs.well	59.8	0.52	6.3E-06	9.0E-10	1.6E-04	7.6E-03	7.8E-03
geomean**				6.4E-06	2.9E-09	1.2E-04	7.1E-03	7.2E-03
StDev (±)				1.0E-07	3.0E-09	4.5E-05	6.7E-04	7.2E-04

853

854

Table 5.

855

856

857

858

Well ID		r (m)	s-max*	K (m/s)	S (-)	NO flow Limit_d1	NO flow Limit_d2
						dist. (m)	dist. (m)
IFP1-6	pump. well	0.11	21.48	5.1E-06	-	20 **	46**
IFP1	obs.well	18.6	20.28	4.0E-06	7.0E-05	31 (10)***	138 (41)***
IFP1-1	obs.well	28.2	11.87	6.0E-06	4.2E-04	35	47
IFP1-2	obs.well	40.4	9.28	5.4E-06	1.6E-04	-	42
IFP1-5	obs.well	17.7	12.69	7.9E-06	1.7E-02	25	44
IFP1-7	obs.well	8.7	14.05	3.3E-06	1.1E-03	16	-
IFP1-9	obs.well	11.5	16.44	3.0E-06	2.6E-03	13	42
IFP1-3	obs.well	61.5	0.75	3.3E-06	8.3E-04	18	43
IFP1-4	obs.well	40.4	0.3	4.8E-05	2.6E-02	-	-
IFP1-8	obs.well	51.7	0.1	1.0E-04	6.3E-02	-	-
BW1	obs.well	69.3	No reaction	-	-	-	-
BW2	obs.well	95.4	No reaction	-	-	-	-
			Average****	4.5E-06	7.8E-04	19.5	44.3
			StDev (±)	1.7E-06	6.0E-03	8.8	2.1

860

861

Table 6.

862

863 **Figures**

864

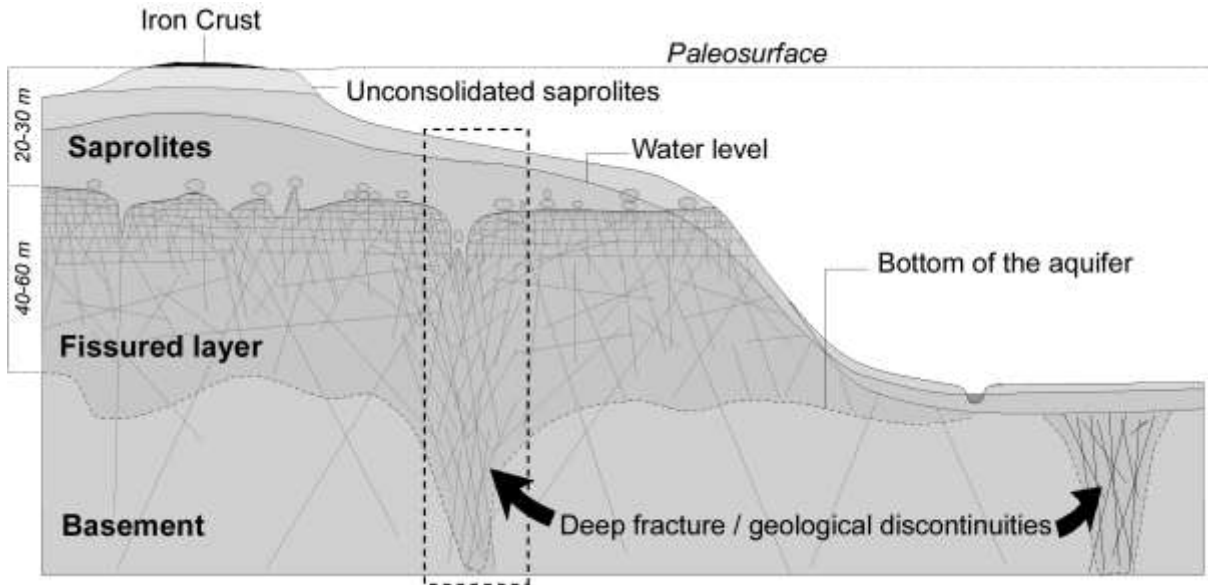


Figure 1

865  
866  
867

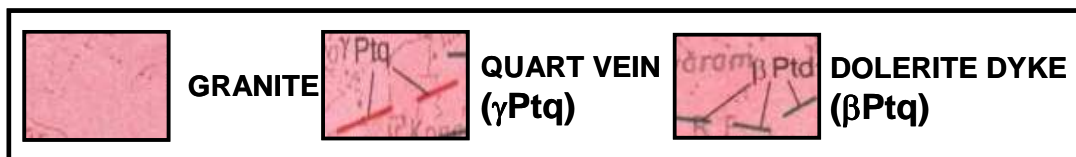
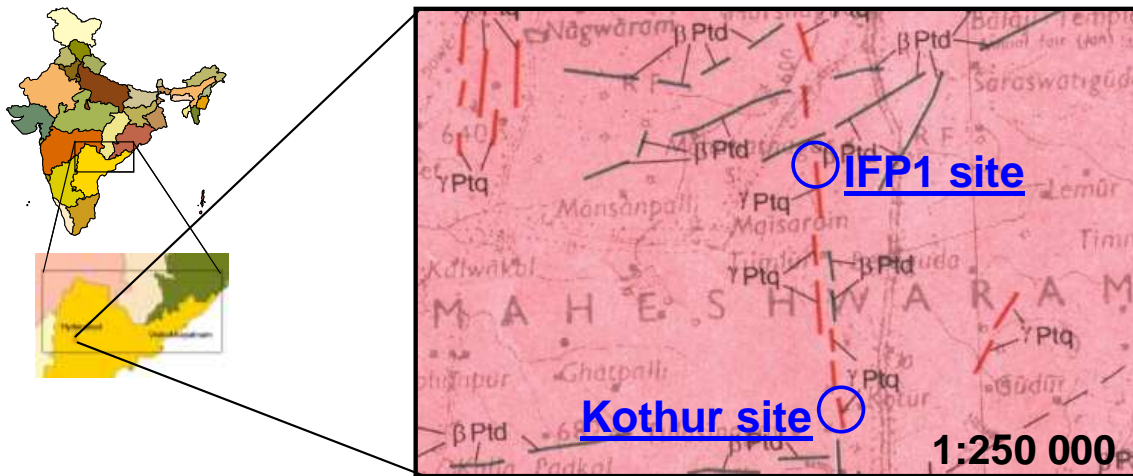
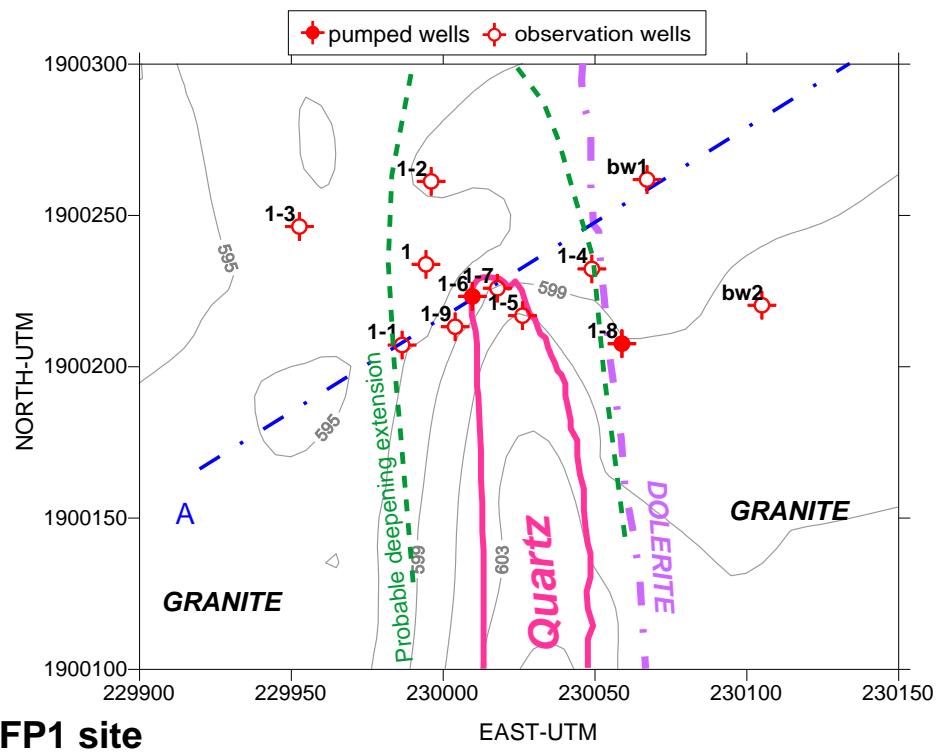
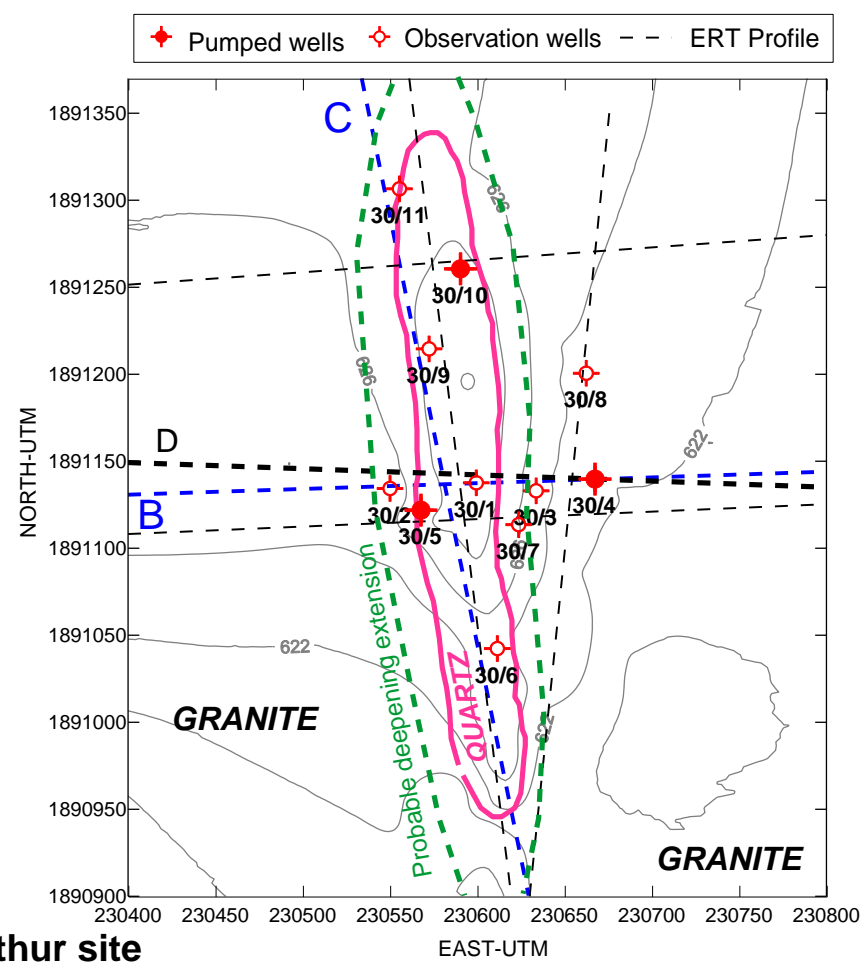


Figure 2

868  
869  
870



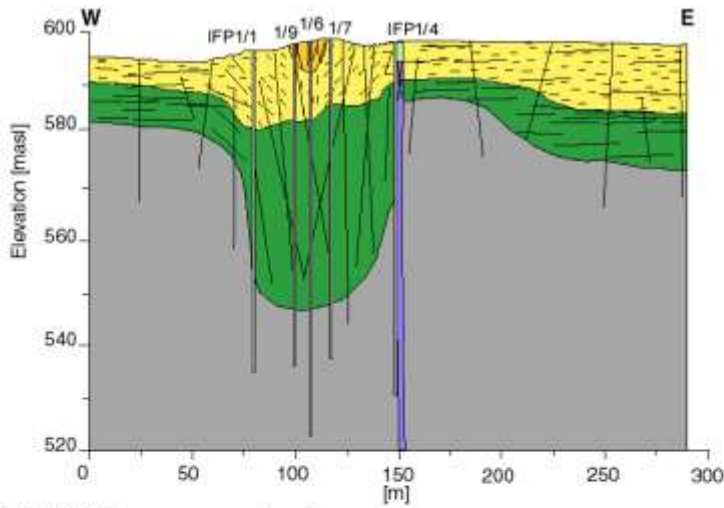
a) IFP1 site



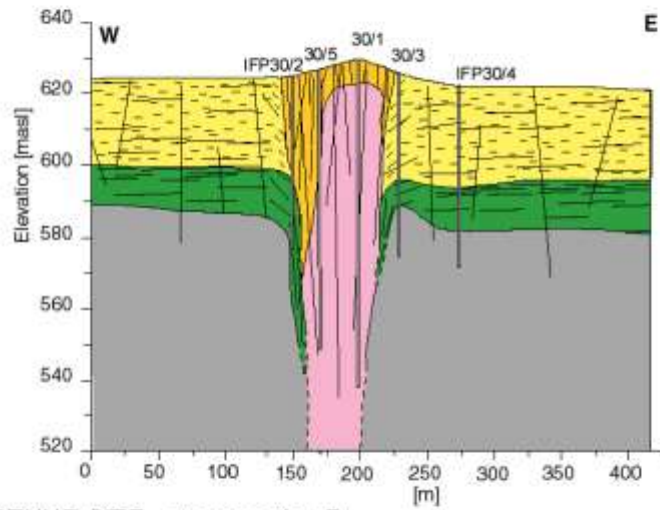
b) Kothur site

Figure 3

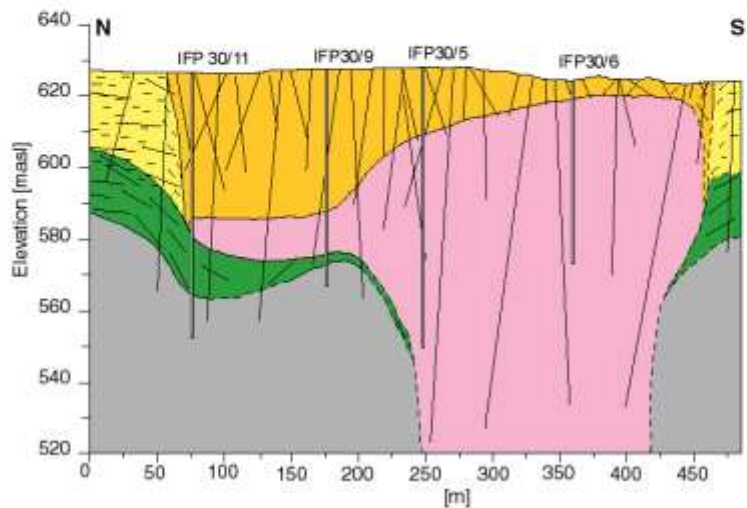
871  
872  
873  
874



a) IFP 1 SITE - cross section A



b) KOTHUR SITE - cross section B



c) KOTHUR SITE - cross section C

**Legend**

Orthogneissic pink granite (porphyritic K-feldspar)	laminated saprolite
fissured layer	unfissured granite
<b>Quartz</b>	
weathered -fissured	fresh -poorly fissured
<b>Dolerite</b>	
weathered-clay	fresh
Fissure	

875  
876  
877  
878  
879

Figure 4.

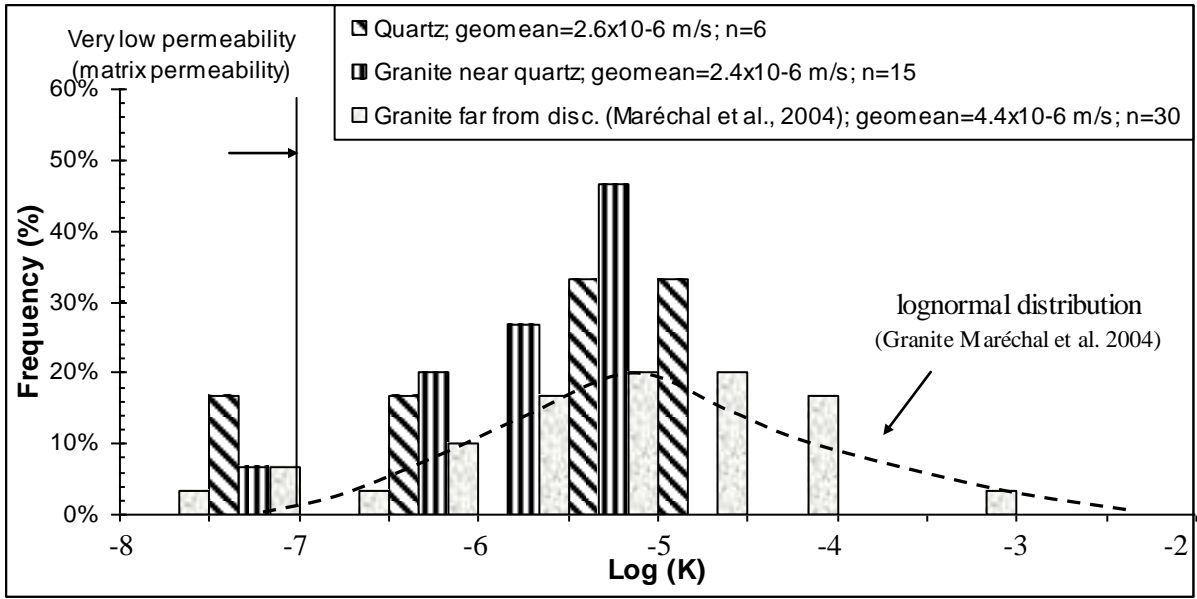
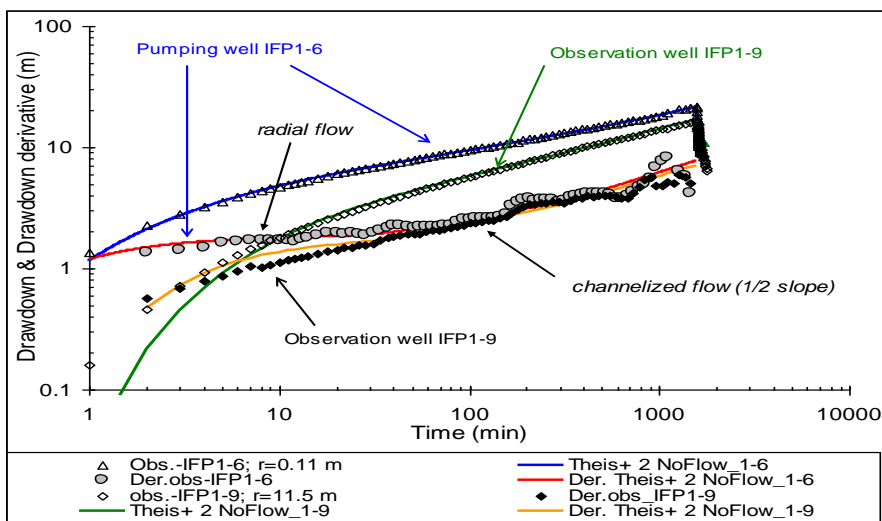
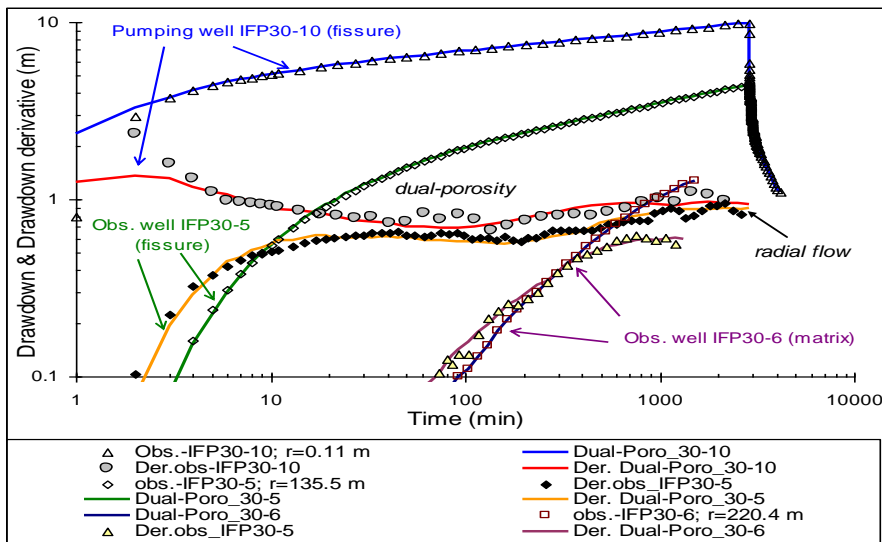
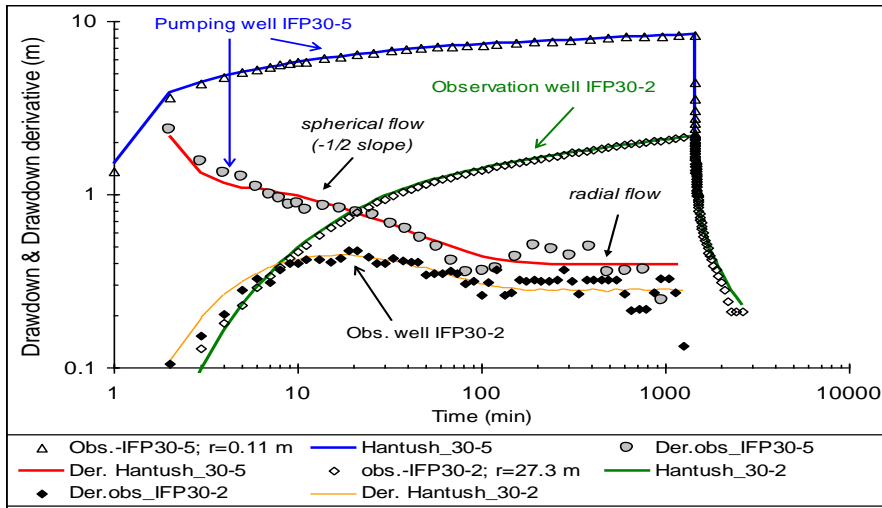


Figure 5.

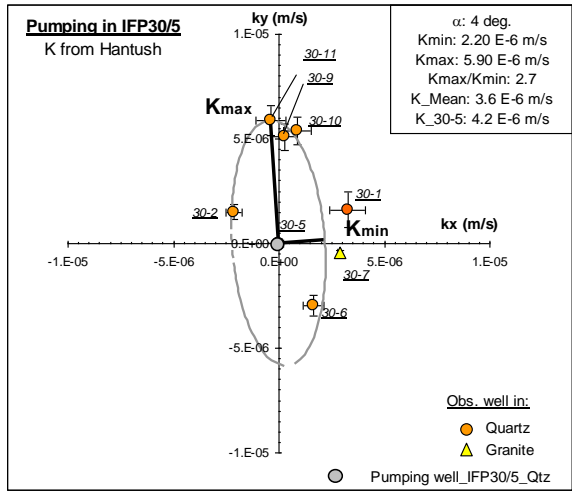
880  
881  
882  
883  
884  
885  
886  
887  
888  
889  
890  
891  
892



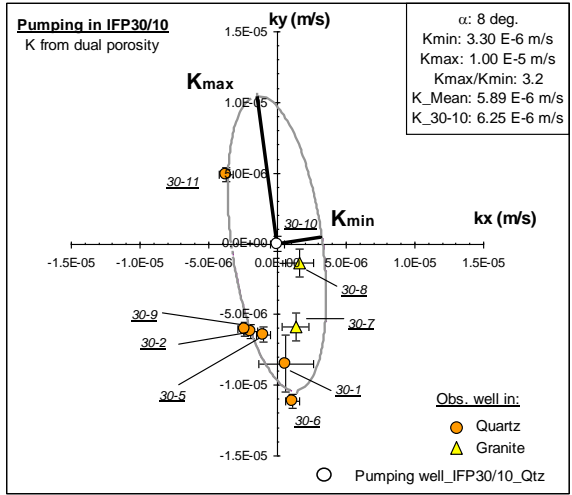
**c) IPF1-6**

Figure 6.

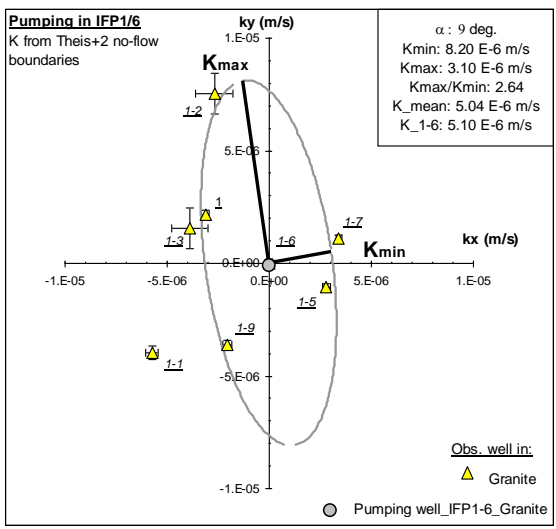
893  
894  
895  
896



**a) IFP30-5 –Kothur site**



**b) IFP30-10 –Kothur site**



**c) IFP1-6 –IFP1 site**

897  
898  
899  
900

Figure 7.

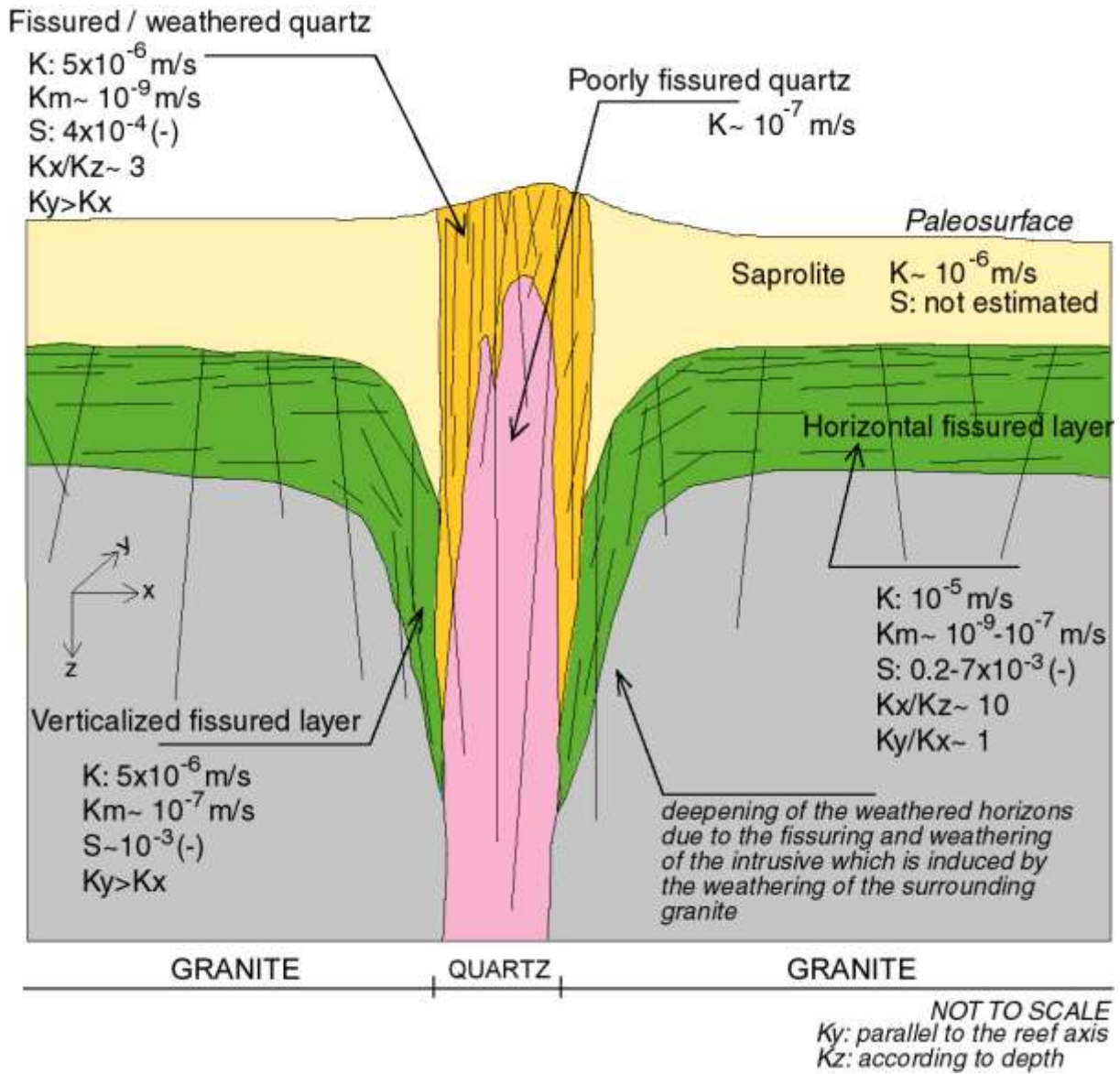


Figure 8.

901  
 902  
 903  
 904